

Detection of Marginal Ice Zone in SAR Imagery using Curvelet based Features: A case study on the Canadian East Coast

Jiange Liu^{a,*}, K.Andrea Scott^b, Paul Fieguth^b

^aDepartment of Automation, Northwestern Polytechnical University, China

^bSystems Design Engineering, University of Waterloo, Canada

Abstract. Monitoring the marginal ice zone (MIZ) is becoming increasingly important due to recent evidence that the width of the MIZ is changing with climate. In this study, a method to automatically detect the MIZ in Synthetic Aperture Radar (SAR) imagery is proposed. The method utilizes the curve-like features of MIZ in SAR images. A multi-scale strategy, the curvelet transform, is chosen to extract features from the SAR images. The statistical and co-occurrence features of curvelet coefficients at an appropriate scale are used to identify the MIZ from open water and consolidated ice. Experimental results show a significant increase in classification accuracy (89.7%) compared with the most commonly used MIZ definition from passive microwave sea ice concentration (74%), especially in the diffuse MIZ.

Keywords: Marginal Ice Zone, SAR Imagery, Curvelet Transform, Curvelet Co-occurrence, SVM.

* Jiange Liu, liujiangecc@163.com

1 Introduction

The marginal ice zone (MIZ) is the transition region from consolidated ice to open water.¹ The MIZ has become increasingly important in recent years toward understanding changes in sea ice cover and ice-ocean-atmosphere interactions.² It is a dynamic region, with ice drift, ice eddies, and wave-ice interaction. MIZs are often regions of intense biological activity and are active areas for fishing and shipping.³

The MIZ is typically defined as the region with sea ice concentration (SIC) between 15% and 80%.^{1,4} The SIC used to estimate the spatial extent of the MIZ are generally obtained from passive microwave brightness temperatures. However, these SIC estimates can be underestimated in regions with low ice concentration.⁵ This may be due to a thin and diffusive ice cover, or due to the use of weather filters in the algorithm. **These filters** may be more likely to be activated in the MIZ **due to increased atmospheric moisture in these regions** . These weather filters result in the sea ice concentration being set to zero when the true ice concentration is relatively low (e.g., 30%),

14 and can remove a significant part of the MIZ.⁶ When the SIC data are used to study trends,⁷ or as
15 observational data for a sea ice forecasting system, this bias is problematic. One way to identify
16 and correct the bias is to use an additional data source that can provide independent information
17 on the sea ice state. Data from synthetic aperture radar (SAR) sensors are useful in this regard.
18 SAR data are not sensitive to atmospheric moisture and can provide information of the surface
19 state at high spatial resolution (e.g., 50m), which is complementary to information from passive
20 microwave instruments.

21 SAR images are typically interpreted manually by operational ice services. This is time con-
22 suming, and results are subjective.⁸ With new and upcoming SAR missions, the quantity of SAR
23 data is rapidly increasing. Methods to automatically interpret the SAR imagery of sea ice are
24 strongly desired. Previous studies in this area include ice-type classification,⁹ ice-water classifica-
25 tion,¹⁰ ice concentration estimation,¹¹ and analysis of ice thickness.^{12,13} Automated detection of
26 the MIZ in SAR imagery has received relatively less attention. One way to identify the MIZ in
27 SAR imagery may be to first estimate the ice concentration from the SAR imagery and then apply
28 thresholds to this concentration. However, methods to estimate SIC from SAR are still a topic of
29 research, and current methods are typically less accurate in the MIZ than in consolidated ice or
30 open water.¹¹

31 In this paper the MIZ is extracted from SAR imagery using a multi-scale method to first com-
32 pute features from the SAR imagery, and then carry out classification using a support-vector ma-
33 chine. Multi-scale methods have been shown to be advantageous for SAR image analysis.¹⁴ In
34 these methods the coarsest scale is the mean value of the input image, while the finest scale is
35 dominated by the image noise. Using the middle scales of the decomposition, it is possible to re-
36 duce the influence of noise and changes in the mean image tone on the classification task. Since the

37 MIZ is characterized by curve-like features with random orientation, in this study the anisotropic
38 curvelet transform is chosen as the multi-scale method. Statistical features of curvelet coefficients
39 and GLCM features of curvelet coefficients at chosen scales derived from SAR images are used to
40 **distinguish** the MIZ from open water and consolidated ice. Note that the superiority of the curvelet
41 approach for MIZ identification has been demonstrated in an earlier study.¹⁵ **Although the method**
42 **is applied to only four SAR scenes in the present study, these scenes have been chosen because**
43 **they represent a range of ice conditions, such as new ice, ice eddies and filaments, and discrete ice**
44 **floes. This allows us to arrive at conclusions regarding the performance of the method for these**
45 **conditions.**

46 The layout of this paper is as follows; in Sections 2 and 3, the data used are described and the
47 feature extraction method is demonstrated. In Sections 4 and 5, the experiments are described and
48 the proposed method is evaluated on four RADARSAT-2 (RS2) SAR images, and compared with
49 the classification result from operational image analysis charts. **Discussion and conclusions are**
50 **given in Sections 6 and 7 respectively.** The results from this study can be used toward **improved**
51 monitoring of the MIZ, which is important for both ice operations and for climate studies.

52 **2 Data and Weather Conditions**

53 *2.1 SAR Imagery*

54 RS2 HH (horizontal transmit and receive) and HV (horizontal transmit and vertical receive) C-
55 band ScanSAR wide beam mode images are used in the present study. This is the **mode that is**
56 frequently used in ice operations. The images have nominal pixel spacing of 50m by 50m and each
57 image is approximately $10,000 \times 10,000$ pixels, covering an area of $500 \text{ km} \times 500 \text{ km}$. Two of
58 the scenes used in the present study are of a dynamic MIZ along the Labrador Coast, and were

59 acquired on February 20th (20110220), and April 5th (20110405), 2011. The other two scenes are
60 from freeze-up in the Gulf of Saint Lawrence, and were acquired on January 17th (20140117) and
61 22nd (20140122), 2014. An example of the SAR scene acquired on February 20th 2011 is shown
62 is shown in Fig.1, with the HH image in panel (a), the HV image in panel (b) and a subset of the
63 image with validation data (discussed in Section 2.2) superimposed in panel (c).

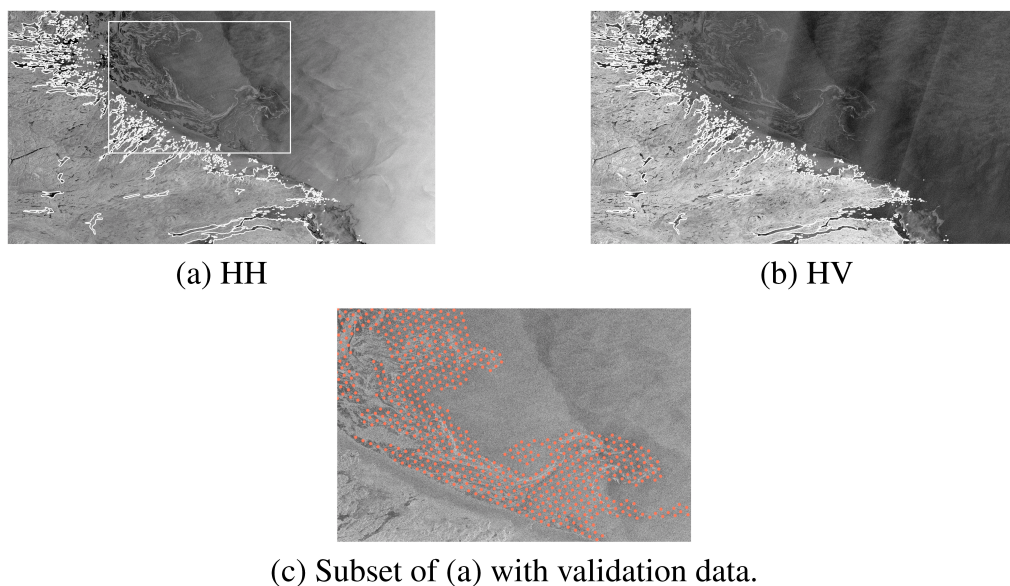


Fig 1 Example image of RADARSAT-2 HH and HV SAR images used in the present study. This image is acquired on February 20th 2011 at 10:12 UTC. Panel (c) shows a zoom in to the region indicated by the box in panel (a) demonstrating the image analysis chart data points corresponding to the MIZ (red).

64 Note that each polarization captures different characteristics of the scene. For example, in
65 Fig.1, some features of the MIZ can be captured in HV, but have a low contrast in the HH image.
66 However, HV images from RADARSAT-2 are known to contain vertical banding noise due to the
67 data processing method used to achieve ScanSAR mode (and this banding can be seen in Fig.1 (b)
68). Furthermore, due to the fact that the signal for the HV image is close to the instrument noise
69 floor, the effect of vertical banding noise can be substantial. This makes it more challenging to
70 automatically extract effective information from this polarization alone. Hence, both HH and HV

71 images are used in the present study, which has been found to give improved results as compared
72 to using either polarization alone in other, similar, studies.¹⁶

73 2.2 Image Analysis Chart

74 Operational image analysis charts are chosen as **validation data** for the classification results. Image
75 analysis charts are manually prepared analyses of SAR imagery generated by expert ice analysts.
76 Using the information in the SAR image, the analyst draws polygons indicating areas where the
77 ice conditions appear to contain a mixture of up to three different ice types. An example of an
78 image analysis chart is shown in Fig.4 (c). The total ice concentration in each polygon is given in
79 increments of 0.1. The MIZ is identified as the area covered by polygons with ice concentration
80 between 0.1 and 0.8. It should be noted that the preparation of image analyses is subjective.⁸
81 Typical errors are positional errors, e.g., polygon boundaries, and error in the interpretation of the
82 SAR imagery. For example, a thin cover of new ice can be dark and featureless and be mistaken
83 for calm open water. Analysts rely on their experience of the imagery and geographic conditions
84 in these cases. In addition, small scale features, such as cracks in the ice cover, are not typically
85 included in image analysis charts.

86 The ice edge in the image analysis charts is considered accurate to within $\pm 500m$ and the
87 ice concentration accuracy is given as $\pm 5\%$.⁸ In practice it is known that the analysts are able to
88 provide a good estimate of the beginning of the MIZ (e.g., 10% SIC contour), and the delineation of
89 the consolidated ice region, but the specific polygon boundaries (e.g., between 40% and 50% SIC)
90 are more subjective. For the present study we use contours of 10% and 80% to delineate the MIZ.
91 Detailed visual inspection of each SAR image with the ice concentration from the corresponding
92 image analysis chart is carried out to assess the accuracy of the image analyses before processing.

93 An example is given in Fig.1 (c). To provide a validation data set, the image analysis chart is
94 interpolated to the SAR image using nearest neighbor interpolation. The value at the corresponding
95 location of the center pixel for each SAR image patch is the label used in the validation data.

96 2.3 Sea ice concentration from passive microwave data

97 The sea ice concentration data is calculated using brightness temperatures from the Advanced
98 Microwave Scanning Radiometer - Earth Observing System instrument on the NASA Earth Ob-
99 serving System (AMSR-E) on Aqua satellite using the ARTIST Sea Ice (ASI)^{17,18} algorithm. The
100 data are mapped to a polar stereographic grid at 6.25 km spatial resolution. In order to use these
101 data with the SAR images, the data are reprojected and interpolated to the SAR image grid. For
102 consistency with the MIZ from the image analysis charts, the MIZ is identified as the region with
103 ice concentration between 0.1 and 0.8. The ASI SIC is chosen because this product is known to
104 have less of a bias under thin ice conditions, which are dominant for the images chosen here, than
105 other sea ice concentration products.¹⁹

106 2.4 Weather and sea ice conditions

107 All of the SAR images used here were acquired off the east coast of Canada at the western boundary
108 of the North Atlantic Ocean and adjoining water bodies. A summary of the weather conditions for
109 each acquisition is given in Table.1. Air temperatures are obtained from the weather station in
110 closest proximity to the image center. The mean, maximum and minimum temperatures given in
111 the table correspond to the values from the twelve hours preceding the image acquisition time.
112 Wind speed and direction are taken from the weather station data, if available. Ice conditions are
113 obtained from an examination of the ice chart on the image acquisition day in addition to those

114 from the proceeding 2-3 days to check the stability of the ice conditions. Note that on all days
 115 except January 17th, 2014, the air temperatures are well below freezing. For the image acquired on
 116 January 17th 2014 it has been verified that, in comparison to previous days, the ice was becoming
 117 thicker and slightly more consolidated in the time leading up to the image acquisition, indicating
 118 freezing conditions.

Table 1 List of weather and sea ice conditions for the four SAR scenes used in this study. NI denotes new ice (thickness less than 10 cm), GI and GWI denote grey ice and grey-white ice (thickness 10-30 cm), FYI denotes first year ice (thickness ranges typically 30-120 cm). Full descriptions of ice types are given in ²⁰.

Image Acquisition date and time (UTC)	Mean air temp (C)	Min air temp (C)	Max air temp (C)	Windspeed (knots) and (direction)	Ice type and features
February 20, 2011 10:12	-4.03	- 5.1	-3.1	15 (N)	GI and GWI with diffuse ice jets, eddies, bands
April 4, 2011 9:52	-13.4	-14.1	-10.7	N/A	medium and thick FYI with floes 50m-500m, diffuse ice near edge
January 17, 2014, 10:39	-0.43	-1.2	1.5	10 (NW)	NI and GI with thin ice eddies
January 22, 2014, 10:24	-14.1	-14.9	-13.3	18 (N)	GWI with NI at the south edge, ice eddies

119 3 Feature extraction method

120 3.1 Motivation

121 The MIZ has a wide span of SIC in addition to the presence of different ice types and ice features,
 122 such as ice floes and ice eddies. To aid our discussion of the MIZ we describe it as consisting
 123 of two zones, one being the compacted marginal ice zone (CMIZ) where the ice concentration
 124 is from 60% to 80% and the second being the diffuse marginal ice zone (DMIZ)²¹ where the ice

125 concentration is from 10% and less than 60%. Examples of these zones in RS2 imagery are shown
 126 in Fig.2 (c,d,e,f) where the zone corresponding to each patch is assigned using the ice concentration
 127 from the image analysis charts.

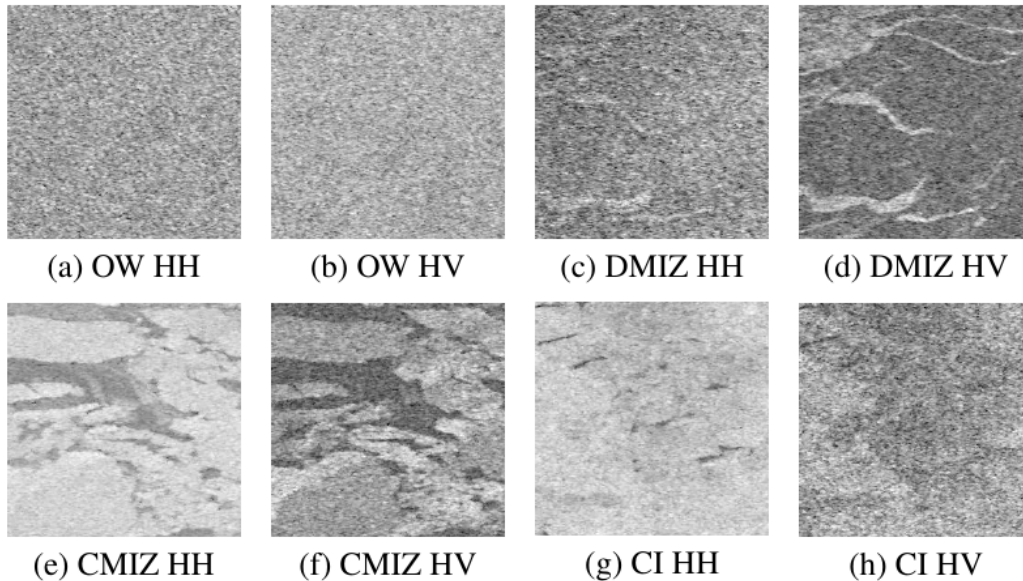


Fig 2 257×257 pixel patch examples of different types considered in this study. (a,c,e,g) are open water (OW), diffuse MIZ (DMIZ), compacted MIZ (CMIZ) and consolidated ice (CI) from HH images. (b,d,f,h) are same types from HV images. Each patch is scaled from 0 to 255 to enhance visualization.

128 From Fig.2, it can be seen that CMIZ (panels e,f) is largely composed of different size of ice
 129 floes, while the DMIZ (panels c,d) may contain more diffuse floes, as well as ice filaments and
 130 ice eddies, where the latter are signatures of thin new ice, and can be called dynamic ice.¹⁵ Note
 131 that the DMIZ is the region in which the ice can be seen as thick curves or filaments at random
 132 orientation. Similarly, in the region of CMIZ, the gaps or leads of open water (or potentially
 133 new ice) among the different sizes of ice floes or pancake ice, also can be expressed as thick
 134 curves of random orientation. Therefore, both the diffuse and compacted MIZ in SAR images
 135 can be considered a region in which curve-like features are dominant. This is in comparison to
 136 consolidated ice (CI, panels g,h) or open water (OW, panels a,b). In particular, it can be seen that

137 the CI and OW patches appear as relatively smooth without many curve-like features at middle
 138 scales. On this basis, the feature extraction in curvelet domain is chosen to identify the MIZ from
 139 other classes in SAR imagery.

140 3.2 Curvelet Transform

141 The curvelet transform gives an optimal sparse representation of singularities along smooth curves
 142 at multiple scales and orientations by scaling and rotating a mother curvelet function.^{22,23} The
 143 rectangle to needle shape mother curvelet function is strongly anisotropic and satisfies the scaling,
 144 $width \approx length^2$ as shown in Fig.3. Instead of the point singularities description of wavelet
 145 transform, the curvelet transform is more suitable to find curve-like features at multiple scales and
 146 any orientation.

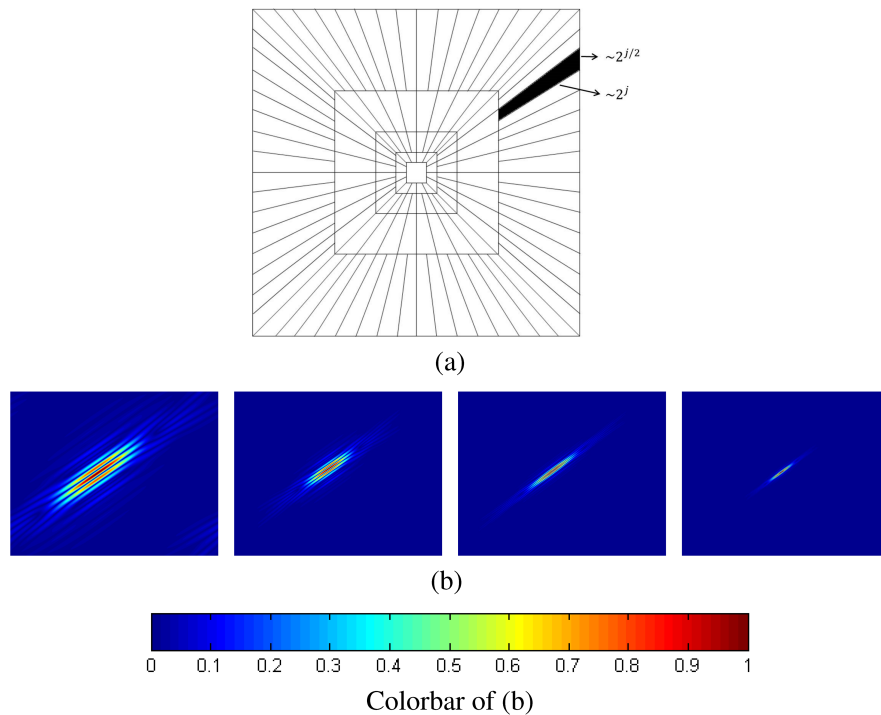


Fig 3 Demonstration of curvelet. (a) Digital (discrete) curvelet tiling in frequency domain satisfying the requirement of $width \approx length^2$ at different scales. (b) Example of the spatial contribution corresponding to a single curvelet coefficient from coarser to finer scales at the same orientation

147 In the present study, the curvelet is implemented in the digital (discrete) domain by the second
 148 generation curvelet transform, following Eq. 1, in which the inner product is taken between the
 149 input Cartesian array $f(x, y)$ with the size of $0 < x, y \leq n$ and the mother curvelet function,
 150 $\varphi_{j,l,K}$, indexed by the scale parameter j , orientation parameter l and a sequence of translation
 151 parameters $K = (k_1, k_2)$, to yield a set of curvelet coefficients $C_{j,l,K}$.²⁴

$$C_{j,l,K} := \sum_{0 \leq x, y \leq n} f(x, y) \varphi_{j,l,K}(x, y). \quad (1)$$

152 The implementation of the curvelet transform in this study follows the fast discrete curvelet
 153 transform (FDCT).²⁴ There are two forms of FDCT which are based on different operations of
 154 Fourier samples, called unequally spaced fast Fourier transform (USFFT) and wrapping based fast
 155 curvelet transform. The difference between these two methods is mainly in the choice of spatial
 156 grid used to translate the curvelet at each scale and orientation. The wrapping based method uses
 157 a regular rectangular grid of size $2^j \times 2^{j/2}$, while USFFT uses a tilted grid. Since the wrapping
 158 based curvelet transform (Eq. 1) is faster in computation time, it is the method used here.

159 In our implementation, the curvelet features are averaged over all orientations at a given scale.
 160 This means an isolated curve, which may correspond to a high value of curvelet coefficient in only
 161 a single orientation, would have a small overall curvelet feature after averaging. For example, leads
 162 in a consolidated ice cover may appear as curves, but they are narrow features with less random
 163 orientation than similar features seen in the MIZ. An image patch with a few isolated leads would
 164 therefore not be identified as MIZ.

165 3.3 Feature Extraction

166 In the present study the wrapping-based curvelet transform method²⁴ is used due to its less redun-
167 dancy and computational efficiency. For this method, the number of scales is determined by the
168 size of the image as Eq.2,

$$n_{scale} = \text{ceil}(\log_2(\min(M, N))) - 3 \quad (2)$$

169 where M, N represents the size of the image. The innermost or the coarsest scale, called scale 1,
170 is not directional, and represents the mean value of the image pixel values. The outermost scale,
171 called n_{scale} , is also not directional and it is the highest frequency (smalles scales) of the image.
172 The details or the curve-like features at different scales are expressed in the intermediate scales with
173 an increasing number of orientations with increasing scale.²⁴ The edges or thin curves in images
174 are captured in the second-to-last scale,²⁵ while the features of thicker curves can be expressed at
175 coarser scales. While the curved features in the SAR imagery correspond to curvelet coefficients
176 with large magnitude, given the intensity and variety of curves within and across a SAR image
177 patch, the value of the curvelet coefficient at a given scale varies considerably. Therefore, it is also
178 of interest to utilize the spatial distribution of the curvelet coefficients. On this basis, curvelet co-
179 occurrence features are also calculated.²⁶ The curvelet co-occurrence features are computed from
180 the grey level co-occurrence matrix (GLCM) where the input image to the GLCM is the magnitude
181 of curvelet coefficient at each scale. There are several curvelet co-occurrence features that could
182 be considered, such as mean, standard deviation, entropy, contrast, homogeneity and so on. To
183 determine the feature set, a forward feature search²⁷ is used. This method begins with an empty
184 set and gradually builds a useful feature set by adding the most useful new feature to the feature

185 set. The feature search stops when additional features no longer increase the value of a defined
 186 utility function. The features obtained using this method for the present study are listed in Table 2.
 187 The selected statistical and co-occurrence features of curvelet coefficients at chosen scale J are the
 mean value for each subband.

Table 2 List of curvelet co-occurrence features selected using a forward search.

Features
Mean
Standard Deviation
GLCM Autocorrelation
GLCM Contrast
GLCM Cluster Prominence
GLCM Dissimilarity
GLCM Energy
GLCM Homogeneity
GLCM Variance
GLCM Mean
GLCM Difference variance

188

189 3.4 Classification

190 The Support Vector Machine (SVM)²⁸ classifier with a radial basis function (RBF) kernel is used
 191 in the proposed method to classify the image into two class: MIZ and others (non-MIZ). The SVM
 192 is a supervised learning method that is used widely in pattern recognition problems. The ability of
 193 SVM classifiers to model a nonlinear decision boundaries make it suitable for our application. The
 194 SVM model in this study is trained and tested using an LOO (Leave One Out) scheme.²⁹ Four SAR
 195 scenes are classified in our experiment. For each scene, training is done on the other three scenes
 196 and testing is done on the scene that has been left out of the training set. This can avoid testing on

197 training data, mimic an operational environment, and give realistic classification accuracy.

198 4 Description of Experiments

199 The experiments are carried out on four RS2 SAR images, two of them are from the Labrador
200 Coast and the other two are from the Gulf of Saint Lawrence. These scenes have a large region of
201 MIZ, and contain significant regions of diffuse ice.

202 The patches over which the image features are calculated should be large enough to contain
203 a meaningful sample of curves. From visual inspection of the curvelet coefficients, those at an
204 intermediate scale of $2^5 = 32$ pixels (1.6 km) are chosen for subsequent processing. According
205 to Eq.2, the patch size should be larger than 256, here, patches of 257×257 pixels (12.8 km \times
206 12.8 km) and the second coarsest scale of curvelet coefficients (called scale 2) are used. Before
207 applying the curvelet transform, both HH and HV image patches are normalized to have values
208 between 0 to 1 and a landmark is applied. Considering the computation time for an entire image,
209 the sliding window method is used to obtain each patch from the image using a 50-pixel-step in
210 both horizontal and vertical directions. In addition, patches containing land, without validation
211 data, or outside the image border, are not used.

212 As discussed in Section 2, the use of both HH and HV images generally provides complemen-
213 tary information that leads to more accurate classifications. To combine information from these
214 two polarizations, we first transform the normalized patch $\bar{I}_{hh}, \bar{I}_{hv}$ of HH and HV separately into
215 the curvelet domain, to obtain C^{hh}, C^{hv} . The fused curvelet coefficients of the HH and HV patches
216 are then obtained by using the higher coefficient magnitude of the same position for each subband
217 at scale 2. The fused curvelet coefficients C^f are used to calculate the curvelet and curvelet co-
218 occurrence features in Table.2. In the construction of the GLCM, 8 grey levels is chosen, and an

219 inter pixel distance of 1 is used when checking the grey level of a pixel against that of its neighbour.

220 The statistics presented are based on averages from four orientations 0° , 45° , 90° and 135° .

221 For each scene, the MIZ is also identified using AMSR-E SIC, curvelet features only, the ice
222 edge from a curvelet approach³⁰ (Labrador coast only), and the SIC estimated from SAR¹¹ (Gulf
223 of Saint Lawrence only).

224 5 Results

225 The classification results are evaluated against the MIZ from the image analysis chart described in
226 Section 2. The total classification accuracy and F1 score³¹ of the confusion matrix entries for each
227 scene are shown in Table.3. It can be seen that the proposed method achieves the highest accuracy
228 and F1 score among the different methods, and there is a 3% – 30% improvement compared with
229 the MIZ from the AMSR-E sea ice concentration. Note that for scene 20110405 and 20140122,
230 about 3/4 of the total image area has a corresponding image analysis.

231 Classification results for the Labrador Coast scenes (20110220 and 20110405) are displayed
232 in Fig.4 and Fig.5. Comparing the results of the MIZ from AMSR-E (Figs.4 (e) and 5 (e)) to
233 the MIZ from the image analysis (Figs.4 (c) and 5 (c)), it can be seen that most of the DMIZ is
234 misclassified as open water by the AMSR-E data. On the other hand, the proposed method is able
235 to correctly classify much more of this region (Figs.4 (h) and 5 (h)). For example, the proposed
236 method achieves a classification accuracy of 97% for the DMIZ for the image acquired on April
237 5th, 2011. For these two images, in addition to the MIZ classification methods using the curvelet,
238 the MIZ is also identified as the region between the curvelet based ice edge detection result³⁰ and
239 the boundary of consolidated ice (SIC = 80%). It can be seen in Table.3 that both the proposed
240 method and the method that extracts the ice edge using the curvelet (region of ice edge and SIC)

241 perform well, with significantly higher F1 scores and accuracy than are achieved with the AMSR-E
242 SIC.

243 However, in cases where the scale of the floe size is much larger than the chosen patch size,
244 since there are few curve-like features inside the patch, the MIZ may be misclassified as consoli-
245 dated ice (black boxes in Fig.5 (h)). Secondly, when the contrast of ice and water of the patch is
246 low in both HH and HV, the MIZ may be wrongly classified into open water or consolidated ice
247 (black box in Fig.4 (h)). In addition, due to the patch size of 257×257 pixels, when the center
248 pixel of patch is open water or consolidated ice and the patch is at the boundary of MIZ/water or
249 MIZ/consolidated ice, the patch may be misclassified (yellow box in Fig.4 (h)).

250 Results from the two scenes acquired during freeze-up in 2014 Gulf of Saint Lawrence are
251 shown in Fig.6 and Fig.7. The first image, shown in Fig.6, corresponds to the beginning of freeze-
252 up, and from the CIS ice chart it is found that most of the ice is very thin (less than 30cm in
253 thickness) on this date. Large regions in the image are incorrectly classified as open water when
254 AMSR-E SIC is used. The total accuracy (Table.3) shows a significant improvement of 30% for
255 the proposed method as compared to the AMSR-E SIC. For the second image, shown in Fig.7,
256 the accuracy of the classification result from AMSR-E SIC has a similar result to the proposed
257 method. The differences are at the ice edge, where the ice is thin new ice (from the CIS ice chart).
258 Finally, note that due to the patch size, when water is surrounded by marginal sea ice, it may be
259 misclassified as MIZ. For these two GSL images, the MIZ is also estimated using SIC retrieved
260 from the RS2 HH and HV SAR images¹¹ using a convolutional neural network (CNN). While the
261 CNN was overall found to produce good estimates of the SIC, the CNN does tend to overestimate
262 the ice concentration in the MIZ, thereby misclassifying the MIZ as consolidated ice (SIC= 100%).
263 Note the CNN¹¹ was trained using image analysis charts.

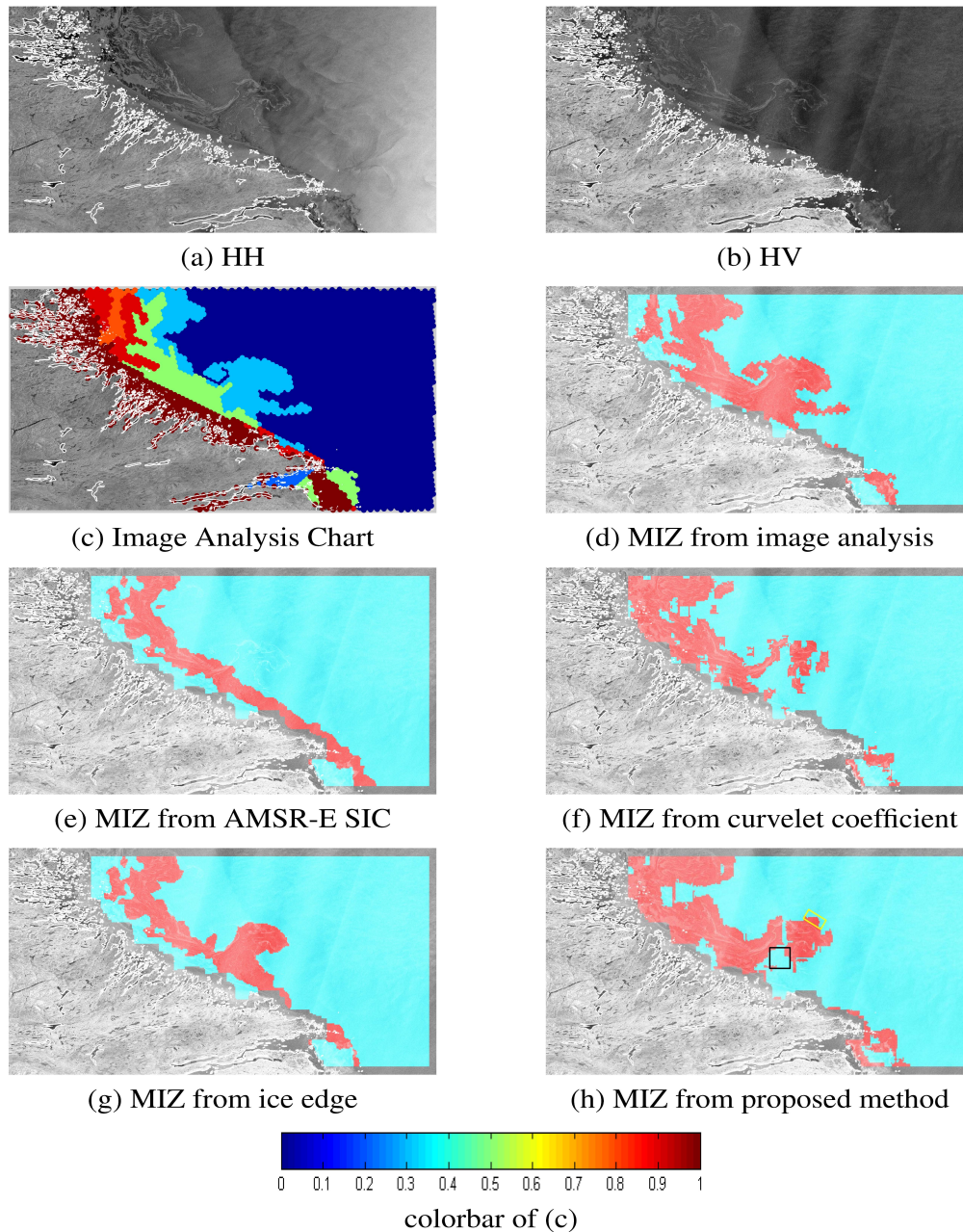


Fig 4 Result analysis of scene 20110220: (a) and (b) are the RS2 SAR HH and HV with white coast line, (c) is the ice concentration from the image analysis chart, (d) HV and **validation data** of MIZ from image analysis chart (c), (e) HV and MIZ definition from AMSR-E, (f) HV and predicted MIZ using statistical features of curvelet coefficients only, (g) HV covered with MIZ definition using ice edge and sea ice concentration boundary between consolidated ice and MIZ of 80%, (h) HV and prediction results of MIZ of proposed method. **The black box in (h) is an example region in the MIZ misclassified into open water due to the contrast of ice and water of the patch being low in both HH and HV. The yellow box in (h) is an example region that misclassified the open water into MIZ at the boundary of two type due to the large patch size.** (From (d) to (h):Classified MIZ is red and others is cyan. The gray pixels are unclassified.)

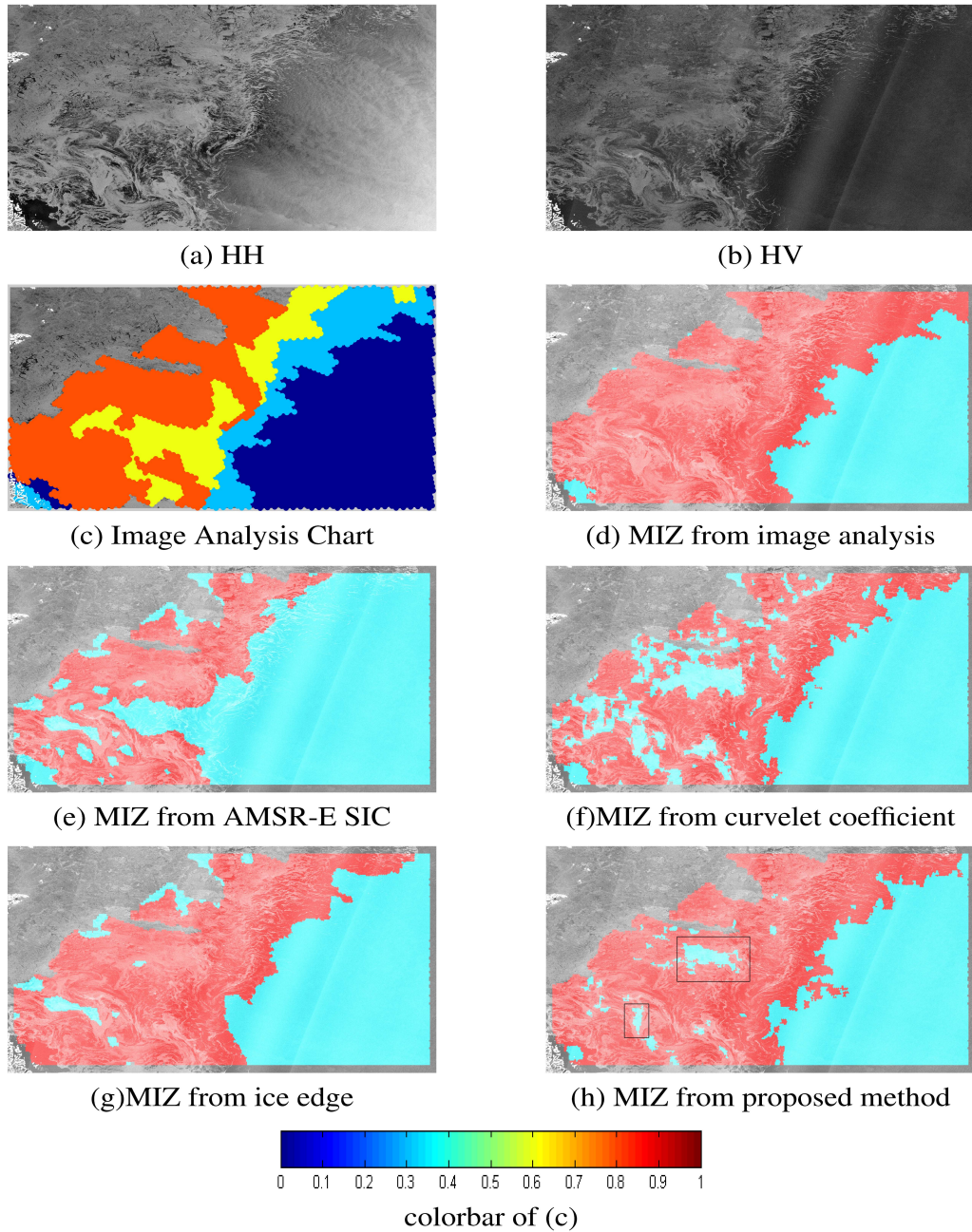


Fig 5 Result analysis of scene 20110405: (a) and (b) are the RS2 SAR HH and HV with white coast line, (c) is the ice concentration from the image analysis chart, (d) HV and **validation data** of MIZ from the image analysis chart (c), (e) HV and MIZ definition from AMSR-E, (f) HV covered with predicted MIZ using statistical features of curvelet coefficients only, (g) HV covered with MIZ definition using ice edge and sea ice concentration boundary between consolidated ice and MIZ of 80%, (h) HV and predicted MIZ from the proposed method. The black boxes in (h) are regions of the MIZ with larger floe sizes than the patch size that lead to misclassification. (From (d) to (h): Classified MIZ is red and others is cyan. The gray pixels are unclassified.)

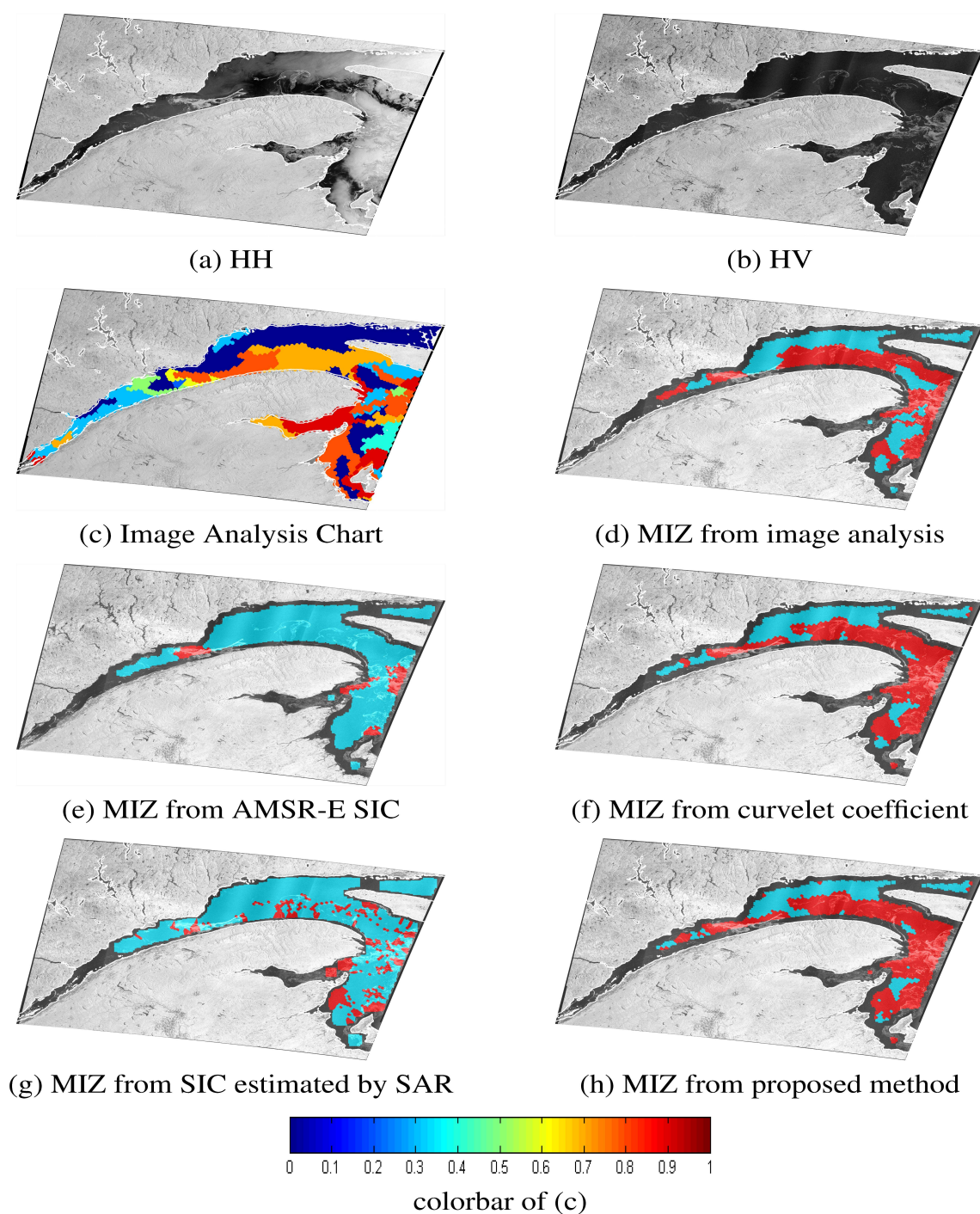


Fig 6 Result analysis of scene 20140117: (a) and (b) are the RS2 SAR HH and HV with white coast line, (c) is the ice concentration from the image analysis chart, (d) HV and **validation data** of MIZ from image analysis chart (c), (e) HV and MIZ definition from AMSR-E, (f) HV and predicted MIZ using statistical features of curvelet coefficients only, (g) HV and MIZ using SIC which estimated by RS2 SAR, (h) HV and prediction results of MIZ of proposed method. (From (d) to (h): Classified MIZ is red and others is cyan. The gray pixels are unclassified.)

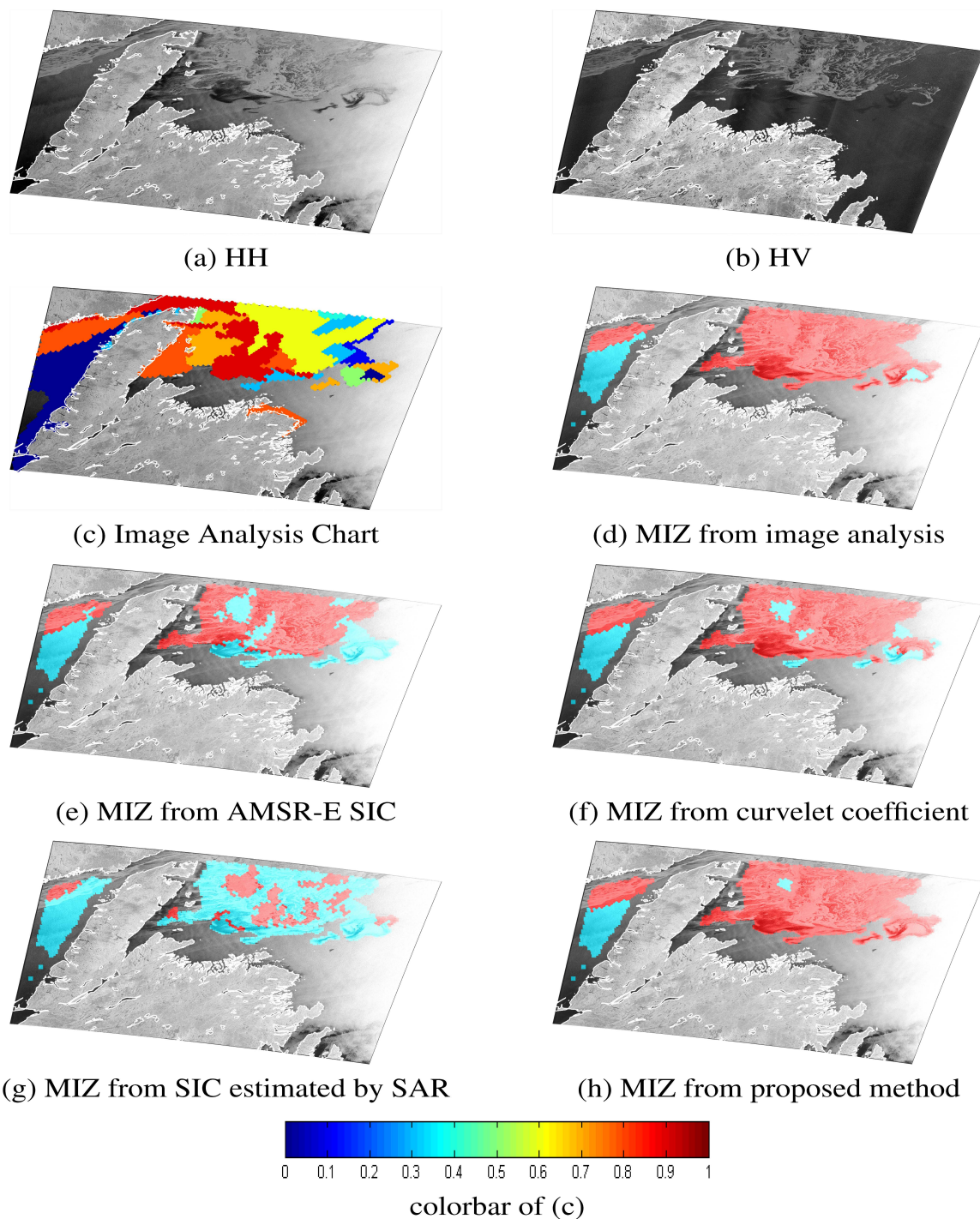


Fig 7 Result analysis of scene 20140122: (a) and (b) are the RS2 SAR HH and HV with white coast line, (c) is the ice concentration from the image analysis chart, (d) HH and **validation data** of MIZ from image analysis chart (c), (e) HH and MIZ definition from AMSR-E, (f) HH and predicted MIZ using statistical features of curvelet coefficients only, (g) HH and MIZ using SIC which estimated by RS2 SAR, (h) HH and prediction results of MIZ of proposed method. (From (d) to (h): Classified MIZ is red and others is cyan. The gray pixels are unclassified.)

Table 3 The total classification accuracy and F1 score of MIZ of different methods for four SAR scenes. Note that the top scores (indicated in bold) are from the proposed method.

20110220	Total Accuracy	F1 score (MIZ)
Sea ice concentration (SIC)	81.6%	0.54
Region of ice edge and SIC	86.9%	0.70
Curvelet	84.0%	0.63
Curvelet+ curvelet co-occurrence	88.8%	0.77
20110405		
Sea ice concentration (SIC)	72.2%	0.71
Region of ice edge and SIC	90.8%	0.92
Curvelet	82.2%	0.84
Curvelet+ curvelet co-occurrence	92.5%	0.93
20140117		
Sea ice concentration (SIC)	52.0%	0.42
SIC from SAR	54.5%	0.46
Curvelet	81.9%	0.86
Curvelet+ curvelet co-occurrence	82.9%	0.87
20140122		
Sea ice concentration (SIC)	91.8%	0.86
SIC from SAR	41.5%	0.51
Curvelet	92.0%	0.95
Curvelet+ curvelet co-occurrence	94.5%	0.97

264 6 Discussion

265 It can be seen in Table.3 that the proposed approach provides accurate classification of the MIZ.
266 Use of the ice edge, also from a curvelet approach,³⁰ is found to work comparatively well (these
267 are entries in Table 3 indicated as 'Region of ice edge and SIC'). However, it is not always straight-
268 forward to define an ice edge, in particular for closed basins, such as the Gulf of Saint Lawrence.

269 From comparison of the classification results with the image analysis ice type information, it
270 is found that in the majority of cases when the MIZ is not estimated accurately from the passive
271 microwave data, the MIZ is characterized by either new ice and/or thin filaments of thicker first
272 year ice. This result is in agreement with other studies.³² It was found that some of these mis-
273 classifications are due to activation of the weather filters, which set the ice concentration to zero
274 in the passive microwave data. For example, 74% of the misclassifications when the PM data are
275 used for the image acquired on January 17, 2014 are from the weather filters. On other dates the
276 fraction is much less, approx 5% to 20%. For new ice, problems can also arise because thin ice has
277 a warmer surface temperature than thick ice, and hence a brightness temperature that is closer to
278 open water. Recalibrating the tie points used in the passive microwave retrieval algorithm³² could
279 lead to improvements, although independent data (e.g., from SAR) would still be need to identify
280 conditions for which recalibration is necessary.

281 The strength of the proposed method lies in its ability to capture the shape and texture of
282 MIZ structures that can be seen in the SAR data. It is not possible to capture the MIZ in SAR
283 imagery from applying a threshold to the SAR backscatter values, due to the complexity of the
284 SAR signatures in these regions. For example, new ice is common in the MIZ, and can be found
285 with either low backscatter, when it is smooth nilas, or high backscatter, when it is either nilas

286 with frost-flowers or pancake ice. The methods here do not threshold backscatter but instead look
287 for patterns in the ice cover that indicate when it is less compact. It is shown that the method
288 performs well in both the diffuse marginal ice zone and new ice conditions, while not leading to a
289 degradation when the MIZ is populated with ice floes and clear continuous curves are less obvious
290 (as in the north-west portion of the image acquired on April 5, 2011). In this latter case both
291 the passive microwave data and the curvelet approach proposed here work well. We note that the
292 testing carried out here is limited. For example, the method was not evaluated on a MIZ populated
293 with multi-year ice floes.

294 **7 Conclusions**

295 The proposed method uses statistical and GLCM features in the curvelet domain for accurate and
296 automatic identification of the MIZ in dual polarization RS2 SAR images. The method is evaluated
297 on four images captured over the Labrador Sea and Gulf of Saint Lawrence. The method achieves
298 an overall accuracy of 89.7%, as compared to a mean overall accuracy of 74% when the MIZ is
299 identified in the passive microwave data. The significant increase in classification accuracy of the
300 proposed method is found in regions where AMSR-E data suffers serious bias errors in the DMIZ
301 with underestimation of the SIC, which leads to misclassification of this region as open water. This
302 bias is not unique to the retrieval algorithm used here, but is common in passive microwave sea ice
303 concentration retrievals.¹ The limitations of the proposed method are at the boundary of MIZ and
304 consolidated ice, which is an ambiguous region even for manual interpretation.

305 As volumes of SAR data are increasing, with the recent Sentinel 1 mission and the upcoming
306 RADARSAT constellation mission, these data will be used increasingly in both operational as well
307 as scientific contexts. At the same time, the number of studies on the MIZ has increased in recent

308 years as this region is expected to become more dominant with changing climate. It is also expected
309 that assimilation of SAR data in operational ice forecasting systems ³³ will be more common in
310 the future. These systems will use the data to retrieve either a continuous ice concentration, or
311 ice water observations, or an ice class (eg. OW/MIZ/CI). Assimilation of this data should lead to
312 more accurate forecasts of the MIZ, with potential benefits for numerical weather forecasts in polar
313 regions.³⁴

314 *Acknowledgments*

315 The RADARSAT-2 data used in this paper was provided by the Canadian Ice Service (CIS). All
316 SAR images are copyright to MacDONALD, DETTWILER AND ASSOCIATES LTD. (2010) -
317 All Rights Reserved.

318 *References*

- 319 1 C. Strong, “Atmospheric influence on Arctic marginal ice zone position and width in the
320 Atlantic sector, February–April 1979–2010,” *Clim. Dyna.* **39**(12), 3091–3102 (2012).
- 321 2 D. Lubin and R. Massom, *Polar Remote Sensing: Volume I: Atmosphere and Oceans*,
322 Springer Science & Business Media (2006).
- 323 3 Y. Jun, Y. Yi, A. K. Liu, *et al.*, “Analysis of sea ice motion and deformation in the marginal
324 ice zone of the Bering Sea using SAR data,” *Int. Journal Remote Sens.* **30**(14), 3603–3611
325 (2009).
- 326 4 J. C. Comiso, “Abrupt decline in the arctic winter sea ice cover,” *Geophysical Res. Letters*
327 **33**(18) (2006).

- 328 5 M. N. Walter, F. Florence, S. J. Scott, *et al.*, “How do sea-ice concentrations from opera-
329 tional data compare with passive microwave estimates? Implications for improved model
330 evaluations and forecasting,” *Ann. Glaciol.* **56**, 332–340 (2015).
- 331 6 N. Ivanova, L. T. Pedersen, R. T. Tonboe, *et al.*, “Inter-comparison and evaluation of sea ice
332 algorithms: towards further identification of challenges and optimal approach using passive
333 microwave observations,” *The Cryosphere* **9** (2015).
- 334 7 J. C. Comiso, W. N. Meier, and R. Gersten, “Variability and trends in the Arctic sea ice cover:
335 Results from different techniques,” *J. Geophys. Res-Oceans* **122** (2017).
- 336 8 G. Crocker, “Canadian ice service digital archive-regional charts: History, accuracy and
337 caveats,” *Canadian Ice Service: Ottawa, ON, Canada* (2006).
- 338 9 N. Y. Zakhvatkina, V. Y. Alexandrov, O. M. Johannessen, *et al.*, “Classification of sea ice
339 types in ENVISAT synthetic aperture radar images,” *IEEE Trans. Geosci. Remote Sens.* **51**(5),
340 2587–2600 (2013).
- 341 10 L. Steven, Z. J. Wang, and C. A. David, “Automated ice–water classification using dual polar-
342 ization SAR satellite imagery,” *IEEE Trans. Geosci. Remote Sens.* **52**(9), 5529–5539 (2014).
- 343 11 L. Wang, A. K. Scott, L. L. Xu, *et al.*, “Sea ice concentration estimation during melt from
344 dual-pol SAR scenes using deep convolutional neural networks: a case study,” *IEEE Trans.*
345 *Geosci. Remote Sens.* **54**(8), 4524 (9) (2016).
- 346 12 L. J. Shi, J. Karvonen, B. Cheng, *et al.*, “Sea ice thickness retrieval from SAR imagery over
347 Bohai sea,” *Geoscience and Remote Sensing Symposium (IGARSS2014)*, 4864–4867 (2014).
- 348 13 J. Karvonen, L. Shi, B. Cheng, *et al.*, “Bohai sea ice parameter estimation based on thermo-
349 dynamic ice model and earth observation data,” *Remote Sens.* **9**(3), 234 (2017).

- 350 14 W. B. Wang, Y. S. Wen, D. Xue, *et al.*, “Sea ice classification of SAR image based on wavelet
351 transform and gray level co-occurrence matrix,” *Fifth International Conference on Instrumen-*
352 *tation and Measurement, Computer, Communication and Control* , 104–107 (2015).
- 353 15 J. G. Liu, A. K. Scott, and P. Fieguth, “Curvelet based feature extraction of dynamic ice
354 from SAR imagery,” *Geoscience and Remote Sensing Symposium (IGARSS2015)* , 3462–
355 3465 (2015).
- 356 16 J. Kavonen, “Baltic sea ice concentration estimated based on C-band dual polarized SAR
357 data,” *IEEE Transactions on Geoscience and Remote Sensing* **52**(9) (2014).
- 358 17 L. Kaleschke, G. Heygster, C. Lupkes, *et al.*, “SSM/I sea ice remote sensing for mesoscale
359 ocean-atmosphere interaction analysis,” *Remote Sens.* , 526–573 (2001).
- 360 18 G. Spreen, L. Kaleschke, and G. Heygster, “Sea ice remote sensing using AMSR-E 89 ghz
361 channels,” *J. Geophys. Res.* , 1–12 (2008).
- 362 19 N. Ivanova, R. Tonboe, and L. T. Pedersen., “SICCI product validation and algorithm selec-
363 tion report (PVASR)455 - sea ice concentration,” *Technical report, European Space Agency*
364 (2013).
- 365 20 D. Fequest, *MANICE: Manual of Standard Procedures for Observing and Reporting Ice Con-*
366 *ditions*, Canadian Ice Service - Environment Canada (2005).
- 367 21 L. Kaleschke and S. Kern, “ERS-2 SAR image analysis for sea ice classification in the
368 marginal ice zone,” *Geoscience and Remote Sensing Symposium (IGARSS2002)* , 3038 –
369 3040 (2002).
- 370 22 J. C. Emmanuel and D. L. Donoho, “Curvelets - a surprisingly effective nonadaptive repre-
371 sentation for objects with edges,” *Astron. Astrophys.* **283**(3), 1051–1057 (2000).

- 372 23 J. Ma and G. Plonka, “The curvelet transform,” *IEEE signal processing magazine* **27**(2),
373 118–133 (2010).
- 374 24 E. J. Candès, L. Demanet, D. L. Donoho, *et al.*, “Fast discrete curvelet transforms,” *Multiscale*
375 *Model. Sim.* **5**, 861–899 (2005).
- 376 25 G. Y. Zhou, Y. Gui, Y. L. Chen, *et al.*, “SAR image edge detection using curvelet transform
377 and Duda operator,” *Electron. Lett.* **46**(2) (2010).
- 378 26 S. Arivazhagan, L. Ganesan, and S. T. G. Kumar, “Texture classification using curvelet statis-
379 tical and co-occurrence features,” *International Conference on Pattern Recognition* **2**, 938–
380 941 (2006).
- 381 27 Guyon, Isabelle, Elisseeff, *et al.*, “An introduction to variable and feature selection,” *J. Mach.*
382 *Learn. Res.* **3**(6), 1157–1182 (2003).
- 383 28 C. Cortes and V. Vapnik, “Support-vector networks,” *Mach. Learn.* **20**(3), 273–297 (1995).
- 384 29 S. S. Keerthi, J. O. Chong, and M. M. S. Lee, “Two efficient methods for computing leave-
385 one-out error in SVM algorithms,” (2000).
- 386 30 J. G. Liu, A. K. Scott, A. Gawish, *et al.*, “Automatic detection of the ice edge in SAR imagery
387 using curvelet transform and active contour,” *Remote Sens.* **8**(6) (2016).
- 388 31 D. M. W. Powers, “Evaluation: From precision, recall and f-measure to ROC, informedness,
389 markedness & correlation,” *J. Mach. Learn. Tech.* **2**, 37–63 (2011).
- 390 32 H. Wiebe, G. Heygster, and T. Markus, “Comparison of the ASI ice concentration algorithm
391 with Landsat-7 ETM+ and SAR imagery,” *IEEE Trans. Geosci. Remote Sens.* **47** (2009).
- 392 33 *Sea ice analysis and forecasting: Towards an increased reliance on automated prediction*
393 *systems*, Cambridge University Press (2017).

394 34 “Atmospheric response to kilometer-scale changes in sea ice concentration within the
395 marginal ice zone,” *Geophysical Research Letters* **45**, 6702.

396 **Jiange Liu** is a Ph.D. candidate at the Northwestern Polytechnical University. She studied at the
397 University of Waterloo as a visiting student during her Ph.D. studies from 2013 to 2015. She
398 received her MS degree in the Department of Automation from the Northwestern Polytechnical
399 University in 2013. Her current research interests include SAR sea ice classification, image analy-
400 sis, and machine learning.

401 **K. Andrea Scott** received the B.A.Sc. and Ph.D. degrees from the University of Waterloo, Wa-
402 terloo, ON, Canada, in 1999 and 2008, respectively, and the M.A.Sc. degree from McMaster
403 University, Hamilton, ON, in 2001. She was a Post-Doctoral Researcher with the Data Assimila-
404 tion and Satellite Meteorology Research Section, Environment and Climate Change Canada, where
405 she was part of a team involved in the development of a sea ice data assimilation system. In 2012,
406 she joined the Department of Systems Design Engineering, University of Waterloo, as a Faculty
407 Member with a specialization in sea ice remote sensing and data assimilation.

408 **Paul W. Fieguth** received the B.A.Sc. degree from the University of Waterloo, Ontario, Canada,
409 in 1991 and the Ph.D. degree from the Massachusetts Institute of Technology, Cambridge, in 1995,
410 both degrees in electrical engineering. He joined the faculty at the University of Waterloo in
411 1996, where he is currently Professor and Department Chair in Systems Design Engineering. His
412 research interests include statistical signal and image processing, hierarchical algorithms, data
413 fusion, and the interdisciplinary applications of such methods. He is the author of a 2010 textbook
414 on Statistical Image Processing and Multidimensional Modelling, and a 2017 textbook on Complex

415 Systems. Biographies and photographs of the other authors are not available.

416 **List of Figures**

- 417 1 Example image of RADARSAT-2 HH and HV SAR images used in the present
418 study. This image is acquired on February 20th 2011 at 10:12 UTC. Panel (c)
419 shows a zoom in to the region indicated by the box in panel (a) demonstrating the
420 image analysis chart data points corresponding to the MIZ (red).
- 421 2 257×257 pixel patch examples of different types considered in this study. (a,c,e,g)
422 are open water (OW), diffuse MIZ (DMIZ), compacted MIZ (CMIZ) and consol-
423 idated ice (CI) from HH images. (b,d,f,h) are same types from HV images. Each
424 patch is scaled from 0 to 255 to enhance visualization.
- 425 3 Demonstration of curvelet. (a) Digital (discrete) curvelet tiling in frequency domain
426 satisfying the requirement of $width \approx length^2$ at different scales. (b) Example of
427 the spatial contribution corresponding to a single curvelet coefficient from coarser
428 to finer scales at the same orientation

429 4 Result analysis of scene 20110220: (a) and (b) are the RS2 SAR HH and HV with
430 white coast line, (c) is the ice concentration from the image analysis chart, (d)
431 HV and validation data of MIZ from image analysis chart (c), (e) HV and MIZ
432 definition from AMSR-E, (f) HV and predicted MIZ using statistical features of
433 curvelet coefficients only, (g) HV covered with MIZ definition using ice edge and
434 sea ice concentration boundary between consolidated ice and MIZ of 80%, (h) HV
435 and prediction results of MIZ of proposed method. The black box in (h) is an
436 example region in the MIZ misclassified into open water due to the contrast of ice
437 and water of the patch being low in both HH and HV. The yellow box in (h) is an
438 example region that misclassified the open water into MIZ at the boundary of two
439 type due to the large patch size. (From (d) to (h):Classified MIZ is red and others
440 is cyan. The gray pixels are unclassified.)

441 5 Result analysis of scene 20110405: (a) and (b) are the RS2 SAR HH and HV
442 with white coast line, (c) is the ice concentration from the image analysis chart,
443 (d) HV and validation data of MIZ from the image analysis chart (c), (e) HV and
444 MIZ definition from AMSR-E, (f) HV covered with predicted MIZ using statistical
445 features of curvelet coefficients only, (g) HV covered with MIZ definition using
446 ice edge and sea ice concentration boundary between consolidated ice and MIZ of
447 80%, (h) HV and predicted MIZ from the proposed method. The black boxes in
448 (h) are regions of the MIZ with larger floe sizes than the patch size that lead to
449 misclassification. (From (d) to (h):Classified MIZ is red and others is cyan. The
450 gray pixels are unclassified.)

- 451 6 Result analysis of scene 20140117: (a) and (b) are the RS2 SAR HH and HV with
452 white coast line, (c) is the ice concentration from the image analysis chart, (d)
453 HV and validation data of MIZ from image analysis chart (c), (e) HV and MIZ
454 definition from AMSR-E, (f) HV and predicted MIZ using statistical features of
455 curvelet coefficients only, (g) HV and MIZ using SIC which estimated by RS2
456 SAR, (h) HV and prediction results of MIZ of proposed method. (From (d) to (h):
457 Classified MIZ is red and others is cyan. The gray pixels are unclassified.)
- 458 7 Result analysis of scene 20140122: (a) and (b) are the RS2 SAR HH and HV with
459 white coast line, (c) is the ice concentration from the image analysis chart, (d)
460 HH and validation data of MIZ from image analysis chart (c), (e) HH and MIZ
461 definition from AMSR-E, (f) HH and predicted MIZ using statistical features of
462 curvelet coefficients only, (g) HH and MIZ using SIC which estimated by RS2
463 SAR, (h) HH and prediction results of MIZ of proposed method. (From (d) to (h):
464 Classified MIZ is red and others is cyan. The gray pixels are unclassified.)

465 List of Tables

- 466 1 List of weather and sea ice conditions for the four SAR scenes used in this study.
467 NI denotes new ice (thickness less than 10 cm), GI and GWI denote grey ice and
468 grey-white ice (thickness 10-30 cm), FYI denotes first year ice (thickness ranges
469 typically 30-120 cm). Full descriptions of ice types are given in .²⁰
- 470 2 List of curvelet co-occurrence features selected using a forward search.

471 3 The total classification accuracy and F1 score of MIZ of different methods for four
472 SAR scenes. Note that the top scores (indicated in bold) are from the proposed
473 method.